

Phase-Engineered Non-degenerate Sliding Ferroelectricity Enables Tunable Photovoltaics in Monolayer Janus $\text{In}_2\text{S}_2\text{Se}$

Yixuan Li^a; Qiang Wang^{a*}; Keying Han^a; Yitong Liang^a; Kai Kong^a; Yan Liang^b; Thomas Frauenheim^c; Xingshuai Lv^d; Defeng Guo^a; Bin Wang^{e*}

^a State Key Laboratory of Metastable Materials Science and Technology and Key Laboratory for Microstructural Material Physics of Hebei Province, School of Science, Yanshan University, Qinhuangdao 066004, People's Republic of China. E-mail: qiangwang@ysu.edu.cn

^b College of Physics and Optoelectronic Engineering, Faculty of Information Science and Engineering, Ocean University of China, Songling Road 238, Qingdao 266100, People's Republic of China.

^c School of Science, Constructor University, 28759 Bremen, Germany; Computational Science and Applied Research Institute (CSAR), Shenzhen518110, P. R. China; Beijing Computational Science Research Center (CSRC), Beijing 100193, P. R. China. E-mail: thomas.frauenheim@bccms.uni-bremen.de

^d School of Science, Shandong University, 250100 Jinan, P. R. China; Beijing Computational Science Research Center (CSRC), Beijing 100193, P. R. China. E-mail: thomas.frauenheim@bccms.uni-bremen.de and

^e Shenzhen Key Laboratory of Advanced Thin Films and Applications, College of Physics and Optoelectronic Engineering, Shenzhen University, Shenzhen, 518060, People's Republic of China. E-mail: binwang@szu.edu.cn

Two-dimensional sliding ferroelectrics, with their enhanced efficiencies of charge separation and tunability, constitute promising platforms for next-generation photovoltaic devices. However, recent systems predominantly exhibit dual degenerate polarization states with weak intensity, hindering the optimal manipulations of photovoltaic effects through sliding ferroelectricity. Here, we address this limitation by introducing two strengthened and distinct non-degenerate sliding ferroelectric phases (WZ' and ZB') in Janus $\text{In}_2\text{S}_2\text{Se}$, which can be achieved by Se-to-S substitution in monolayer In_2Se_3 . First-principles calculations validate the experimental synthesis of this structure and its capability for reversible phase transitions triggered by atomic layer sliding, and series of superior photovoltaic performances are demonstrated in such unique Janus $\text{In}_2\text{S}_2\text{Se}$, accompany with a detailed analysis of how non-degenerate sliding ferroelectricity modulates distinct photovoltaic characteristics. The WZ' to ZB' transition can increase the carrier mobility and tunes the band gap into a more moderate and indirect-to-direct character, yielding a marked red-shift and enhancement of photocurrent peak in infrared spectrum. Conversely, the WZ' phase, benefiting from enhanced polarization, delivers superior photoelectric conversion efficiency in the visible light region. This work establishes a phase-engineered framework of how non-degenerate sliding ferroelectricity orchestrates distinct photovoltaic behaviors, and the intrinsic physical correlations may offer novel perspectives for next designing and regulating innovative photovoltaic devices.

I. INTRODUCTION

Two-dimensional excitonic solar cells (2D XSCs), due to its intrinsic potential for low-cost, eco-friendly, and highly efficient photo-electric conversion surpass the conventional bulk ones, is considering as ideal candidates to address recent environmental and energy crises.¹ In these thin films, photo-generated carriers are generated upon illumination, and then separated under varying interfacial electron ionization and affinity potentials. To date, the rapid exciton recombination remains a critical bottleneck limiting the power-conversion efficiency in 2D XSCs.² One promising strategy is integrating ferroelectricity and photovoltaics into a single system,³ in which the spontaneous out-of-plane polarization (OOP) can effectively inhibit carrier recombination, thereby improving their photoelectric conversion efficiencies.^{4,5} Recent theoretical and experimental evidences have also demonstrated this assertion.^{6,7} However, naturally oc-

curring 2D ferroelectric materials are exceedingly rare due to the stringent symmetry requirements.⁸ Exploring novel formation mechanisms of 2D ferroelectricity and deciphering its role in amplifying photovoltaic responses are essential to enhance the photovoltaic metrics in next-generation of 2D XSCs.

2D sliding ferroelectrics, with the OOP polarization generated by interlayer asymmetric stacking, enabling nonpolar monolayers to acquire switchable dipoles through interlayer sliding, thus can vastly broadens the pool of 2D ferroelectrics.⁹ Such concept is initially proposed theoretically in 2017¹⁰, and has been experimentally implemented since 2021.^{9,11} Owing to the robust structure, easy experimental operation, high Curie temperatures and fatigue-free switching,¹² making them attractive for memory and actuator applications.¹³ Besides, the built-in polarization fields in these materials can drive superior photovoltaic effects, enabling enhanced charge separation,¹⁴ intrinsic type-II band

alignments,¹⁵ above-band-gap photovoltages¹⁶ and enhanced photoelectric conversion efficiencies over the limitation of Shockley-Queisser¹⁷ in 2D devices. Despite these advances, significant challenges remain in realizing ideal 2D sliding ferroelectric photovoltaic systems: One is the insufficient polarization magnitudes resulting from weak interlayer vdW coupling,¹⁸ which impedes the efficient separation of photo-generated carriers; The other refers to the presence of dual degenerate polarization states,^{18,19} impossible to explore the intrinsic correlations between ferroelectricity and photovoltaic effects. Further efforts should be focus on the materials design and scalable assembly techniques to unlock the full potential of sliding ferroelectrics in photovoltaics.

Monolayer $\alpha - In_2Se_3$, featured by a corrugated quintuple-layer honeycomb structure composed of alternating Se-In-Se-In-Se atomic layers, is an ideal representative that integrates ferroelectricity and photovoltaics.^{20,21} Since the built-in asymmetry breaks its OOP inversion symmetry, enabling robust spontaneous OOP polarization in this emerging monolayer, which is still switchable via atomic layer sliding of middle Se.²² Recent theoretical and experimental studies have demonstrated series its photovoltaic superiorities, including the narrow band gap (~ 1.45 eV),²³ the above-band-gap photovoltages,²⁴ and the photocurrents two orders of magnitude higher than bulk ferroelectrics.²⁵ The ultrafast and nonvolatile photocurrent hysteresis²⁰ further highlights its potential for integrated optoelectronics and all-optical signal processing. More inspiringly, this special material is also confirmed to share two distinct ground states, namely ZB' and WZ' ,²¹ offering more versatile ferroelectric characteristics for photovoltaic modulation.

Janus monolayers, with the two faces bear different atomic species or chemical terminations, exhibit stronger OOP dipoles due to the intensified broken of inversion symmetry.²⁶ This asymmetric structure is first realized in transition-metal dichalcogenides by selective replacement of one chalcogen face,²⁷ synthetic routes now extend to oxides,²⁸ halides,²⁹ and rare-earth compounds.³⁰ Inspired by these systems, the Janus $\alpha - In_2Se_3$ can be realized by substituting layers of Se atoms with the homotopic S. Compared to pristine $\alpha - In_2Se_3$, this Janus one ought to exhibit enhanced charge separation capabilities due to the asymmetrical bilateral atoms and stronger OOP dipole. In addition, such asymmetric structure also gives rise to two non-degenerate polarization states between ZB' and WZ' , enable more adjustable polarization intensities and photovoltaic characters during their sliding transition. Therefore, we can wonder more controllable and superior photovoltaic performances in this newly predicted Janus monolayer, and further exploring the underlying correlation mechanisms between 2D sliding ferroelectricity and photovoltaics.

Here, the In_2S_2Se is chosen because of its optimal band gap and superior carrier mobility among Janus various Janus In_2Se_3 monolayers.³¹ First-principles calcula-

tions confirm its structural, dynamic and thermal stability. Compared to the pristine $\alpha - In_2Se_3$, its enhanced bilateral asymmetry yields stronger out-of-plane polarization and more efficient charge separation, driving improved photovoltaic performance. More strikingly, we demonstrate two non-degenerate sliding-ferroelectric phases, ZB' and WZ' , which can be reversible via interlayer sliding at experimentally accessible energy barriers. Further detailed analysis of its regulation effects on photovoltaics are conducted, where the WZ' to ZB' transition red-shifts and amplifies the infrared photocurrent peak, while the WZ' phase delivers higher conversion efficiency under visible illumination. Together, these results establish a phase-engineered link between 2D sliding ferroelectricity and tunable photovoltaics, paving the way for next-generation 2D optoelectronic devices.

II. MODEL AND NUMERICAL METHOD

For the periodic system of Janus In_2S_2Se , the crystal relaxation, structural stabilities, electronic properties and light absorption coefficients were simulated by using the Vienna ab initio simulation package (VASP), which is based on density functional theory (DFT).³² The exchange correlation functional of Perdew–Burke–Ernzerhof (PBE) level was used to deal with the geometrical optimization and electronic structure self-consistent calculations within the generalized gradient approximation (GGA).³³ To address the underestimation of band gap at PBE level, the more accurate results were calculated based on the hybrid density functional of Heyd–Scuseria–Ernzerhof (HSE06), and the Hartree–Fock exchange energy was set 25%.³⁴ To expand the electron wave function into plane waves, the projector augmented wave (PAW) approach was employed with a plane wave cut off energy of 500 eV.³⁵ The convergence criteria were $0.01 \text{ eV}\text{\AA}^{-1}$ for force and 10^{-5} eV for energy, a k-point mesh of $15 \times 15 \times 1$ was used to sample the Brillouin zone, and a vacuum larger than 20 Å was used to eliminate the spurious interactions perpendicular to the 2D plane. In addition, the dynamic stability for each phase was confirmed by the phonon spectrum, which was calculated by using the Nanodcal code. The thermal stability was verified by performing an ab initio molecular dynamics(MD) simulation within a $4 \times 4 \times 1$ supercell under 300 K, the evolution time was set 5 ps with a time step of 1 fs. The energy barriers during the sliding ferroelectric switching were calculated under the method of nudged elastic band (NEB), with the direction and intensity of OOP polarization were evaluated combining the approaches of voltage drop and Bader charge analysis.

The simulations of In_2S_2Se based two-probe nanodevices were performed by using the first-principles quantum transport package Nanodcal,^{36,37} which is based on the combination of non-equilibrium Green's function and DFT (NEGF-DFT).³⁶ During our calculation, the gen-

eralized gradient approximation at PBE level was used to handle the exchange-correlation potential, the wave functions were expanded by the basis sets using atomic orbitals of double-zeta polarization (DZP), the norm-conserving non-local pseudo-potential was applied to define the atomic core, and the energy convergence criterion of self-consistence was set to be less than 10^{-5} eV.³² Besides, a k-mesh grid of 64×1 for center and 256×1 for the leads were set perpendicular to the transport direction during the self-consistent and photocurrent computations.

III. NUMERICAL RESULTS AND DISCUSSIONS

A. Structure, stability and OOP polarization of b-In₂S₂Se

The fully optimized In₂S₂Se structures under *WZ'* (a) and *ZB'* (b) states are displayed in Fig. 1 (a-b), where two Se atomic layers are substituted by the homotopic S. According to the different layers of atomic substitution, each state exhibits three distinct configurations: *t* – In₂S₂Se, *m* – In₂S₂Se, and *b* – In₂S₂Se (Fig. S1). To obtain the most stable configuration, the binding energy for each structure is calculated using the formula: $E_b = (E_{\text{total}} - nE_{\text{In}} - mE_S - kE_{\text{Se}}) / (m + n + k)$, where E_{total} , E_{In} , E_S and E_{Se} represent the energies of monolayer material, a single In atom, S atom and Se atom. As shown in Table S1, the E_b of different stacking In₂S₂Se can be reached 1.1–1.2 J/m², larger than the typical 2D MoS₂, GaTe, and Bi₂O₂Se, indicating their energy feasibility. Considering the lower E_b of *b* – In₂S₂Se than others within each state, these two configurations are selected for further investigation. To examine the experimental feasibility of these two *b* – In₂S₂Se monolayers, their phonon spectrum and *ab initio* molecular dynamics simulations are conducted in Fig. S2. Firstly, the phonon spectra contains no virtual frequencies over the entire Brillouin zone, indicating stable minimum values of these two monolayers on potential energy, hence both of them are all dynamically stable.³⁸ Additionally, to explore the thermal stability of these two monolayers, the temporal evolution of their total energy are also simulated in Fig. S2 (c-d). For each structure, the total energy fluctuates around a constant value with minimal amplitude. After 5 ps of evolution and, only slight changes in atomic configurations occur, with no obvious geometry reconstruction or bond breaking. This confirms that these two In₂S₂Se monolayers maintain stability at elevated room temperature. These stability characteristics suggest robust feasibility for the experimental preparation of both *WZ'* and *ZB'* In₂S₂Se, and provide solid basis for their further sliding ferroelectric and photovoltaic related characters investigation.

Inspired by the sliding ferroelectricity in monolayer

In₂Se₃, we wonder whether it can be maintained in the Janus In₂S₂Se. As illustrated in Fig. 1 c, via specific middle and bottom atomic layers sliding, the phase transition between *WZ'* and *ZB'* states can be achieved in this Janus In₂S₂Se. The evolution energy barrier along the reaction path is ~ 60 meV, which is experimentally achievable and consisted with that of monolayer In₂Se₃ (66 meV)²¹. Owing to the atomic asymmetry inherent to its dual-sided composition, enhanced OOP polarization intensities can be detected in such Janus In₂S₂Se, which can be reached $P_{WZ'} = 14.16 \text{ pCm}^{-1}$ under *WZ'* state and $P_{ZB'} = -11.51 \text{ pCm}^{-1}$ under *ZB'* state, higher than the typical monolayer α – In₂Se₃ (10 pCm^{-1}),³⁹ bilayer BN (2.0 pCm^{-1})⁹ and MoS₂ (2.2 pCm^{-1})⁴⁰ systems under identical computational conditions.

To verify the distinct directions and intensities OOP polarization of this Janus In₂S₂Se, the electrostatic potentials under different states along Z axis are displayed in Fig. 1 (d-f). The potential energy decrease $\Delta\Phi$ are 1.6 eV for *WZ'* state and -1.3 eV for *ZB'* state, which is non-degenerated and higher than those of monolayer α – In₂Se₃, reinforcing the stronger and non-degenerate OOP sliding ferroelectricity. Interestingly, not only such enhanced OOP polarization in Janus In₂S₂Se may resulting in superior photovoltaic performances, the non-degenerated OOP ferroelectric states can also provide a new regulated strategy of sliding ferroelectric on photovoltaics.

B. Photovoltaics related Electronic characters of b-In₂S₂Se

Next, the electric properties between *WZ'* and *ZB'* In₂S₂Se are investigated in-depth to explore their photovoltaic superiority. Firstly, the band structures, projected density of states (PDOS) and partial charge densities are comparatively studied in Fig. 2 (a-b). Obviously, with the sliding phase transition from *WZ'* to *ZB'*, an indirect-to-direct behavior occurs accompany with a decrease of band gap. When in *WZ'* state, the band gap are 2.19 (1.42) eV at HSE06 (PBE) level, which is too larger for visible-light absorption,⁴¹ let alone the non-beneficial of indirect band gap on the production of photogenerated charge carriers.⁴² Inspiringly, when the phase is transferred into the *ZB'*, a moderate direct band gap of 1.17 (0.54) eV at HSE06 (PBE) level can be obtained, which perfectly fits the optimum range for excitonic solar cells (1.2–1.6 eV).⁴³ Another critical factor of 2D photovoltaic candidates is the capabilities of real space charge separation. As shown in the middle and right panels of Fig. 2 (a-b), obvious charge separation behaviors can be observed both states of the Janus In₂S₂Se. For *WZ'* state, the conduction band minimum (CBM) is dominated by the bottom Se layer, the valence band maximum (VBM) is mainly contributed by the top and middle S layers, while under *ZB'* state, the CBM and VBM are mainly dominated by the top S and bottom Se layers, respectively. In-

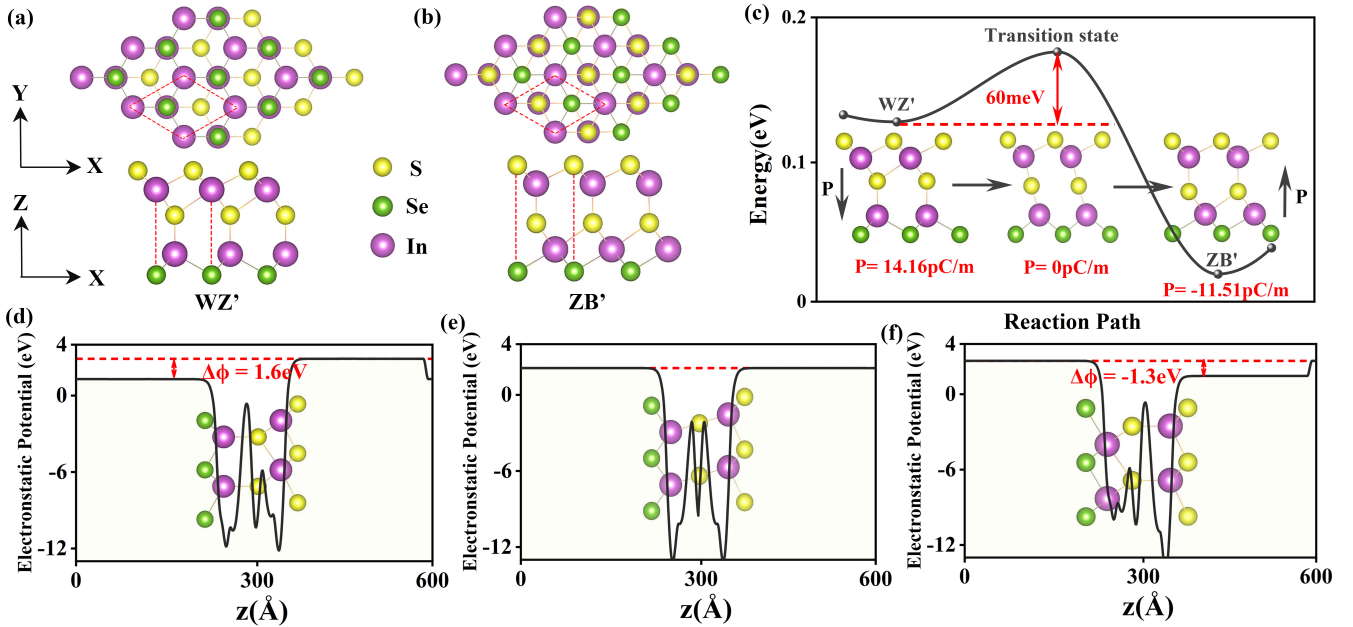


FIG. 1. (a-b) Top and side views of schematic structures of monolayer b-In₂S₂Se under WZ' (a) and ZB' (b) states. In each panel, the red diamond represents the size of one unit cell, with S, Se, and In atoms distinguished by yellow, green, and purple spheres. (c) Energy variation of b-In₂S₂Se along the out-of-plane ferroelectric switching pathway under NEB simulation. The three inserts depict configurations at the initial, middle, and final states, with P indicating the corresponding OOP polarization strength. (d-f) Plane-averaged electrostatic potentials along the Z axis for b-In₂S₂Se at different states.

deed, these distinct charge separation behaviors between the two states are driven by their intrinsic opposite OOP polarization, and further affecting their photovoltaic performances. In Fig. 2 (c-d), the charge density differences between the two states are displayed. Obviously opposite and significantly enhanced charge transfer across the plane can be detected of the WZ' state than ZB', and consisting with the more accurate Bader charge results, where the charge transfer under WZ' and ZB' states are 2.114 and -2.107, respectively. So far, the opposite direction and stronger intensity on OOP polarization of the WZ' than ZB' state are confirmed, which may further demonstrate different photovoltaic performances.

To explore the different carrier mobilities (μ_{2D}) of monolayer Janus $\alpha - In_2Se_3$ between WZ' and ZB' states, the μ_{2D} of these two states are calculated according to the following express based on the DP theory, which has been widely used to simulate the μ_{2D} of 2D crystals:⁴⁴

$$\mu_{2D} = \frac{eh^3 C_{2D}}{k_B T |m_{e/h}^*| E_1^2} \quad (1)$$

where E_1 denotes the variable state, $m_{e/h}^*$ is the effective mass of electrons/holes, T is the temperature, k_B is the Boltzmann constant, and C_{2D} indicates elastic modulus for each state crystal. The obtained results are displayed in Table s2, where μ_{2D} of Janus In₂S₂Se are obvious higher than those in monolayer $\alpha - In_2Se_3$,³¹ suggesting superior photovoltaic performances of the for-

mer. More interestingly, since higher μ_{2D} of ZB' than WZ' state can be obtained, enhanced photocurrent in it based nano-device is also predicted. Over all, by expanding monolayer $\alpha - In_2Se_3$ to the Janus In₂S₂Se, we not only propose a photovoltaic system with superior performances, but can also achieve effective regulations of non-degenerate sliding ferroelectricity on photovoltaics in a single monolayer system.

C. Photocurrent differences between WZ' and ZB' b-In₂S₂Se based nano-devices

Despite excellent photovoltaic characters of WZ' and ZB' In₂S₂Se have been confirmed, they are only provides qualitative predictions due to the constraints imposed by periodic boundary conditions. To further explore their actual excellence in practical devices, it is essential to account for quantum scattering under open boundary condition. Therefore, WZ' and ZB' In₂S₂Se based nano-devices are designed according to Fig. 3 (a). For each device, both leads are constructed by periodically extending the scattering region, and such simplified device model has proven to be effective and optimal in series previous theoretical and experimental research.⁴⁵

During our calculation, the entire scattering region was illuminated by linearly polarized light perpendicular to the plan. A minute bias voltage of 0.2 eV is applied between source and drain, which is far less than the band gap and only intended to drive the photocurrent. Under

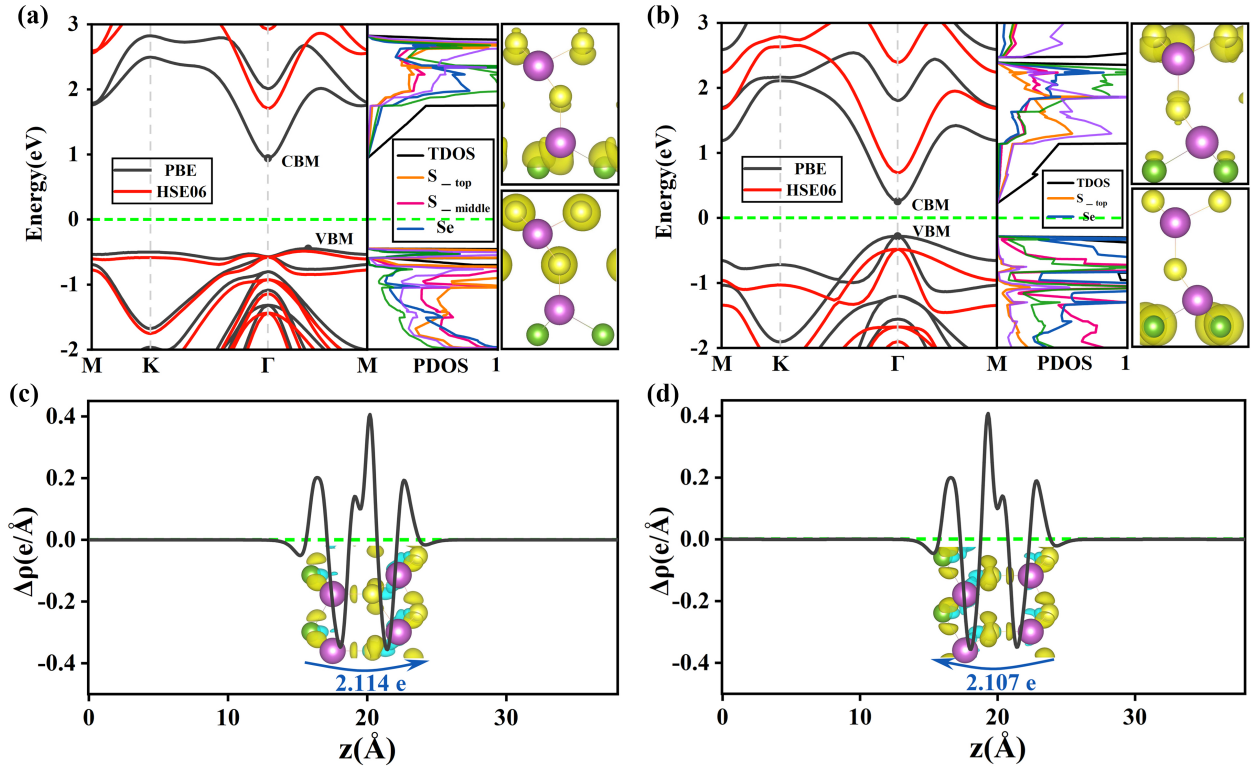


FIG. 2. (a-b) The calculated band structures (left panel), PDOSs (middle panel), and partial charge densities at CBM and VBM (right panel) for b-In₂S₂Se under WZ' (a) and ZB' (b) states. In each panel, the band curvess at PBE and HSE06 levels are distinguished by black and red lines, the fermi level is set to zero and marked by the green dashed line, and the isosurface value in the right panel is set at 0.015eÅ⁻³. (c-d) 3D isosurface and 2D integrated charge density differences along Z axis of b-In₂S₂Se under WZ' (c) and ZB' (d) states, with isosurface value being set at 0.005eÅ⁻³, the charge accumulation and dissipation are indicated by green and orange balls, respectively.

the first-order of Born approximation, the photocurrent ingress into the left probe can be expressed as:^{46–48}

$$I_L^{ph} = \frac{ie}{h} \int \text{Tr} \left[\Gamma_L \{ G^{<(ph)} + f_L(E)(G^{>(ph)} - G^{<(ph)}) \} \right] dE \quad (2)$$

where f_L is the Fermi distribution function of the left lead, $G^{>/<(ph)}$ represents the greater/lesser Green's function, indicating the electron-photon interaction, and Γ_L is the line-width function, signifying the coupling between the left lead and the central scattering region. The calculated photocurrent density $J_L^{ph} = I_L^{ph}/S$ with polarization angle $\theta = 0^\circ$ are displayed in Fig. 3 (b). For both states, J_L^{ph} start to vibrate when the incident light energy E_{ph} increases to the value of band gap, subsequently increasing rapidly. Series of inspiring photovoltaic behaviors can be achieved between these two states. Firstly, significant peak values of J_L^{ph} can be obtained under both states, with the magnitudes can be reached 10.79 μAmm^{-2} and 8.42 μAmm^{-2} for WZ' and ZB' states. Such efficient J_L^{ph} peak values are higher than those of monolayer In₂Se₃ (3.95 μAmm^{-2}) under the same basis of calculation,⁴⁹ which is consistent with the above predictions in Fig. 2 (c-d) and can be illustrated by the

enhanced OOP polarization perfectly. Besides, enlarged J_L^{ph} of WZ' than ZB' state can be detected within the visible light region, Indicating its higher solar photovoltaic conversion efficiency. To delve into the intrinsic motivations, the light absorption, photogenerated carrier separation and transport characters are compared and analyzed in-depth. As shown in Figure 3(c), the absorption coefficients are approximately consistent throughout the entire light range of E_{ph} , including the infrared, visible light, and ultraviolet regions, effectively eliminating the influence of light absorption on the difference of J_L^{ph} between the two states. In fact, such different solar photovoltaic conversions between WZ' than ZB' states is closely related to their distinct OOP polarization as we have discussed in Fig. 1(c), where the intensified OOP polarization will drive more efficient separation of photo-generated carriers, so is the enlarged J_L^{ph} in the visible light region. Except the magnitude of J_L^{ph} , the E_{ph} positions of their peak are also different form Fig. 3 (b), where the peak value of J_L^{ph} appears at $E_{ph} = 2.41$ eV for WZ' state and 2.21 eV for ZB' state. These different peak positions can be attributed to the distinct density of state between the two devices. As shown in Fig. 3 (d), the E_{ph} gaps between the two initial peaks near the fermi

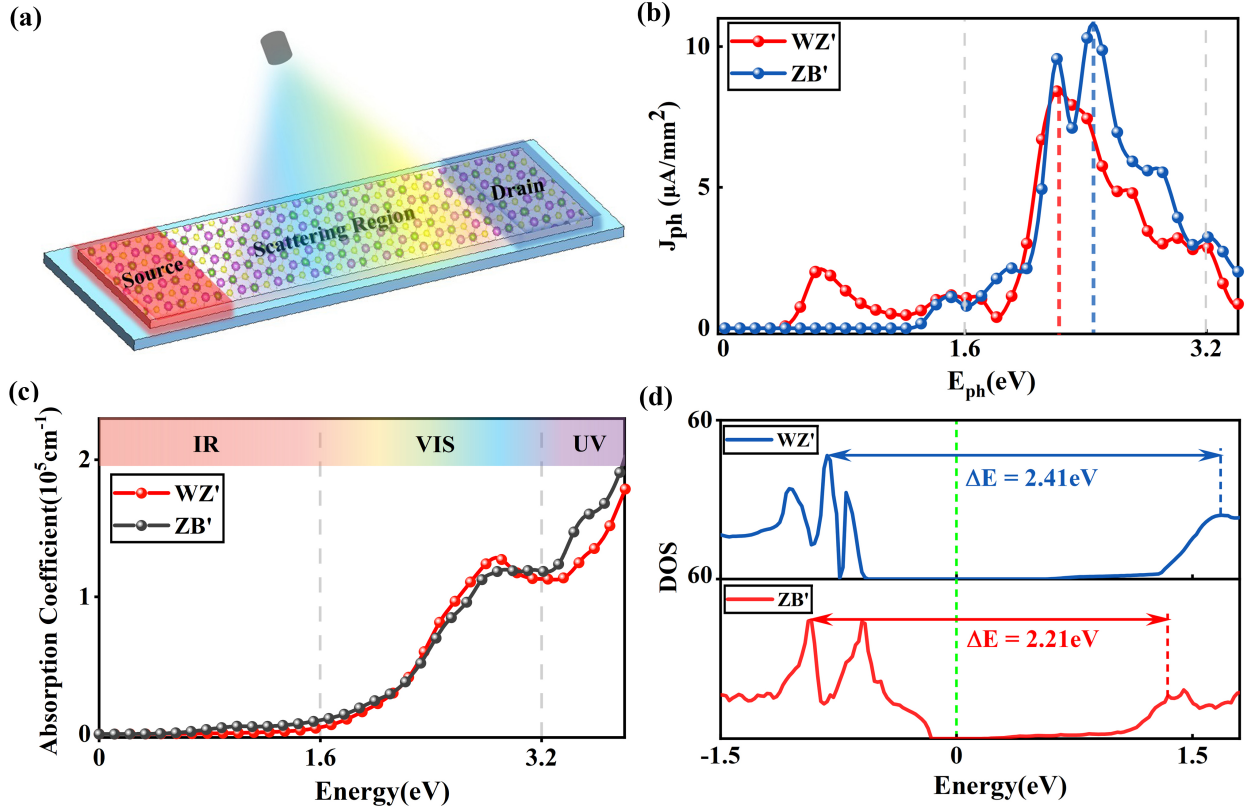


FIG. 3. (a) Schematic diagram of a two-probe PV device for the monolayer b-In₂S₂Se. (b) At $\theta = 0^\circ$, the J_{ph} versus incident light energy E_{ph} of the devices under WZ' and ZB' states. (c) Optical absorption coefficients $a(\omega)$ versus incident light energy E_{ph} of WZ' and ZB' states. The visible light region lies between the two vertical dashed lines. (d) Density of devices states (DOS) of the WZ' and ZB' devices versus energy.

energy are also 2.41 eV for WZ' state and 2.21 eV for ZB' state. The enhanced density of states can provide favorable guarantees for effective carrier transmission, and ultimately resulting in the peak of J_L^{ph} . Furthermore, a significantly enlarged and red-shifted peak value of J_L^{ph} is observed of ZB' than WZ' state within the infrared region. The red-shift phenomenon can be attributed to the reduced band gap in the ZB' state, which facilitates earlier oscillations of J_L^{ph} . Additionally, the augmented peak value of J_L^{ph} is associated with the transition from an indirect to a direct band gap, as well as higher carrier mobilities in the ZB' state relative to the WZ' state.

Moreover, distinguished evolution behaviors of J_L^{ph} versus θ can be obtained between each state of Janus In₂S₂Se, as shown in Fig. 4 (a). When $E_{ph} = 3.11\text{eV}$ reversed shapes of J_L^{ph} curves can be observed, where J_L^{ph} of ZB' state follows the sinusoidal distribution but alongs a cosine one under the WZ' state; while at $E_{ph} = 2.61\text{eV}$, both curves obey the cosine distributions. These different evolution shapes can be reasonably illustrated by the following reformed expression of J_L^{ph} according to Ref. [

47]:

$$\begin{aligned} J_L^{ph} = & \frac{ie}{h} \int \\ & \left\{ \cos^2\theta \text{Tr} \left[\Gamma_L \{ G_1^{<(ph)} + f_L(E)(G_1^{>(ph)} - G_1^{<(ph)}) \} \right] \right. \\ & + \sin^2\theta \text{Tr} \left[\Gamma_L \{ G_2^{<(ph)} + f_L(E)(G_2^{>(ph)} - G_2^{<(ph)}) \} \right] \\ & + \sin(2\theta) 2 \text{Tr} \left[\Gamma_L \{ G_3^{<(ph)} + f_L(E)(G_3^{>(ph)} - G_3^{<(ph)}) \} \right] \\ & \left. \} \times dE, \right. \end{aligned} \quad (3)$$

where the J_L^{ph} is dissected into three components, which are proportional to $\sin^2\theta$, $\cos^2\theta$, and $\sin 2\theta$, respectively. Indeed, the morphological evolution of J_L^{ph} bears a profound correlation with the corresponding crystal lattice symmetry, and can be dominated by the coefficients competition between each trigonometric functions. To elucidate further distinctions in solar photovoltaic performance between the WZ' and ZB' phases of In₂S₂Se, Fig. 4 (b-c) illustrates their θ depended J_L^{ph} distributions entire the visible light region. In both states, the maximum peaks of J_L^{ph} are located at $\theta = 0^\circ$, accompany with a marginal red-shift in peak position occurs in

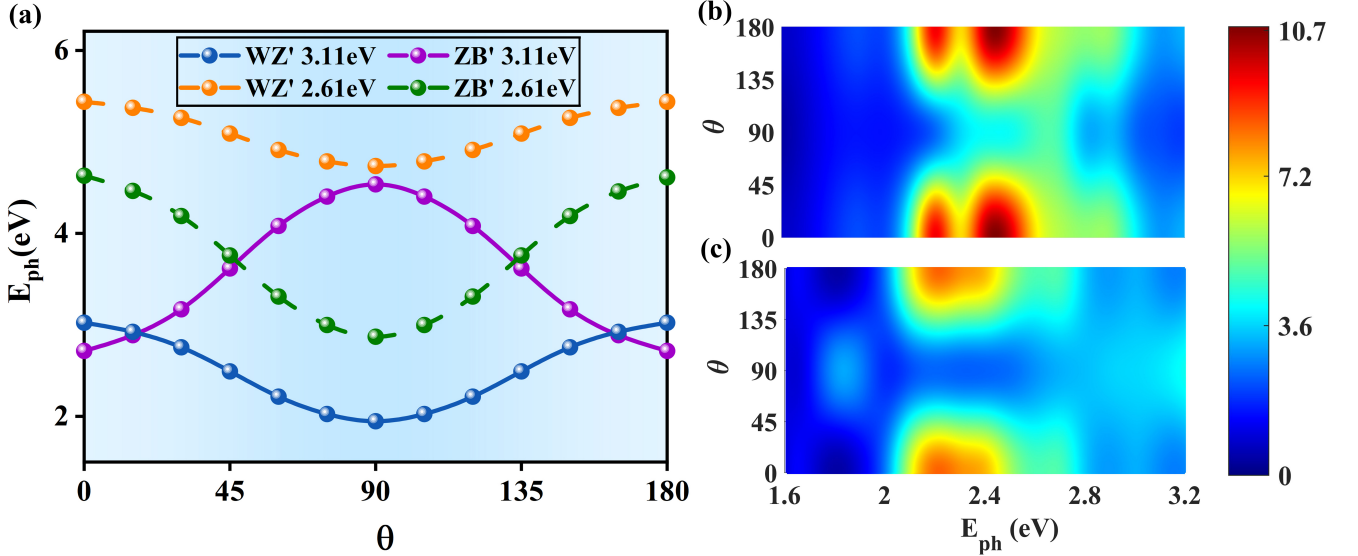


FIG. 4. (a) The J_{ph} versus θ at $E_{ph} = 3.11\text{eV}$ and $E_{ph} = 2.61\text{eV}$ of the WZ' and ZB' state devices. Photocurrent density J_{ph} versus incident light energy E_{ph} and polarization angle θ , for WZ' (b) and ZB' (c) state at the PBE level.

ZB' state. Once again, such distinct peak positions are consisted with the ΔE between the two nearest peaks within the device's density of states in Fig. 3 (d). Besides, a notably elevated and broader J_L^{ph} peak can be observed in the WZ' state, suggesting its superior efficacy in solar energy conversion compared to the ZB' ones. This enhancement is ascribed to the intensified OOP polarization in the WZ' structure, which finally intensifies the separation of photo-generated carriers, a pivotal factor in photovoltaic performance. Remarkably, all above distinct excellent characters of J_L^{ph} can be regulated via switching the two states of in Janus In_2S_2Se by sliding ferroelectricity, which is usually easier to be operated than traditional ferroelectrics in experiments.^{50,51}

IV. DISCUSSION

In summary, to address the limitations of recent 2D sliding ferroelectrics in photovoltaic enhancements, we have proposed Janus In_2S_2Se as a robust platform for establishing effective modulations of photovoltaics via non-degenerate sliding ferroelectricity. Due to the increased asymmetry of surface atoms, two distinct phases and stronger OOP dipoles can be realized in this Janus In_2S_2Se than monolayer $\alpha - In_2Se_3$, thereby behaving superior and controllable photovoltaic related characteristics. we show that both phases of this Janus In_2S_2Se are experimental feasible, and can be switchable via low-barrier ($\sim 60\text{meV}$) interlayer sliding. When compared to the conventional $\alpha - In_2Se_3$ monolayer, stronger OOP polarization, higher carrier mobilities, more efficient light absorption and lower exciton binding energy can be de-

tected in Janus In_2S_2Se , hence enhanced J_L^{ph} can be obtained in their based nano-devices. Besides, we have also demonstrate the phase-dominant modulation of photovoltaic properties in this new predicted Janus In_2S_2Se . The WZ' to ZB' transition increases carrier mobilities and shifts the band gap from indirect toward direct character with more moderate size, producing a pronounced red-shift and enhanced J_L^{ph} in the infrared spectrum. Conversely, duo to the enhanced OOP polarization in WZ' phase, superior J_L^{ph} in the visible light region is delivered during the ZB' to WZ' transition, indicating its more efficient solar photovoltaic conversions. Overall, by leveraging phase-engineered sliding ferroelectricity in Janus In_2S_2Se , we introduce a feasible physical correlations between sliding ferroelectricity and photovoltaics, and the insight mechanisms may shed new light on conception and modulation of next ultrathin and switchable photovoltaic devices.

CONFLICTS OF INTEREST

The authors declare no competing financial interest.

ACKNOWLEDGEMENTS

This work was financially supported by grants from the Natural Science Foundation of Hebei province (Grant No. E2019203163); Innovation Capability, Improvement Project of Hebei province (Grant No. 22567605H); Cultivation Project for Basic Research and Innovation of Yanshan University of China (Grant No. 2021LGQN017); Shenzhen Natural Science Foundations (Grant No. JCYJ20190808150409413), and the Young Talents Project at Ocean University of China.

- ¹ J.-P. Correa-Baena, M. Saliba, T. Buonassisi, *et al.*, Promises and challenges of perovskite solar cells, *Science* 358 (2017) 739–744.
- ² J.-C. Blancon, H. Tsai, W. Nie, *et al.*, Extremely efficient internal exciton dissociation through edge states in layered 2d perovskites, *Science* 355 (2017) 1288–1292.
- ³ M. Kruse, U. Petralanda, M. N. Gjerding, *et al.*, Two-dimensional ferroelectrics from high throughput computational screening, *npj Comput Mater* 9 (2023) 45.
- ⁴ H. Zarenezhad, S. D. e Asl, F. Uçar, *et al.*, Suppressing charge carrier recombination in halide perovskite solar cells by ferroelectric polarization, *J. Mater. Chem. C* 13 (2025) 3372–3381.
- ⁵ Y. Yuan, T. Reece, P. Sharma, *et al.*, Efficiency enhancement in organic solar cells with ferroelectric polymers, *Nature Mater* 10 (2011) 296–302.
- ⁶ Y. Li, J. Fu, X. Mao, *et al.*, Enhanced bulk photovoltaic effect in two-dimensional ferroelectric *cuinp₂s₆*, *Nat Commun* 12 (2021) 5896.
- ⁷ X. Chen, K. Xu, T. Qin, *et al.*, Bulk photovoltaic effect in a two-dimensional ferroelectric semiconductor $\alpha - \text{in}_2\text{se}_3$, *Nanoscale* 17 (2025) 5005–5011.
- ⁸ S. Jiang, Y. Wang, G. Zheng, Two-dimensional ferroelectric materials: From prediction to applications, *Nanomaterials* 15 (2021) 109.
- ⁹ K. Yasuda, X. Wang, K. Watanabe, *et al.*, Interfacial ferroelectricity by van der waals sliding, *Science* 372 (2021) 1458–1462.
- ¹⁰ L. Li, M. Wu, Binary compound bilayer and multilayer with vertical polarizations: Two-dimensional ferroelectrics, *ACS Nano* 11 (2017) 6382–6388.
- ¹¹ M. V. Stern, Y. Waschitz, W. Cao, *et al.*, Interfacial ferroelectricity by van der waals sliding, *Science* 372 (2021) 1462–1466.
- ¹² J. Xing, Y. Tang, J. Li, *et al.*, Intrinsic out-of-plane and in-plane ferroelectricity in 2d *agcrs₂* with high curie temperature, *Adv. Mater.* 36 (2024) 2407655.
- ¹³ R. Bian, R. He, E. Pan, *et al.*, Developing fatigue-resistant ferroelectrics using interlayer sliding switching, *Science* 385 (2024) 57–62.
- ¹⁴ R. Kabe, C. Adachi, Organic long persistent luminescence, *Nature* 550 (2017) 384–387.
- ¹⁵ J.-J. Zhang, D. Zhu, B. I. Yakobson, Heterobilayer with ferroelectric switching of topological state, *Nano Letters* 21 (2021) 785–790.
- ¹⁶ L. Tan, F. Zheng, S. Young, *et al.*, Shift current bulk photovoltaic effect in polar materials—hybrid and oxide perovskites and beyond, *Science* 2 (2016) 16026.
- ¹⁷ S. Yang, J. Seidel, S. Byrnes, *et al.*, Above-bandgap voltages from ferroelectric photovoltaic devices, *Nature Nanotech* 5 (2010) 143–14.
- ¹⁸ M. Wu, J. Li, Sliding ferroelectricity in 2d van der waals materials: Related physics and future opportunities, *PNAS* 118 (2021) e2115703118.
- ¹⁹ P. Meng, Y. Wu, R. Bian, *et al.*, Sliding induced multiple polarization states in two-dimensional ferroelectrics, *Nat Commun* 13 (2022) 7696.
- ²⁰ Z. Lei, J. Chang, Q. Zhao, *et al.*, Ultrafast photocurrent hysteresis in photoferroelectric $\alpha - \text{in}_2\text{se}_3$ diagnosed by terahertz emission spectroscopy, *Science Advances* 11 (2025) eads8786.
- ²¹ W. Ding, J. Zhu, Z. Wang, *et al.*, Prediction of intrinsic two-dimensional ferroelectrics in *in₂se₃* and other iii₂-vi₃ van der waals materials, *Nat Commun* 8 (2017) 14956.
- ²² Y. Zhou, D. Wu, Y. Zhu, *et al.*, Out-of-plane piezoelectricity and ferroelectricity in layered $\alpha - \text{in}_2\text{se}_3$ nanoflakes, *Nano Letters* 17 (2017) 5508–5513.
- ²³ L. Z. J. He, T. Li, *et al.*, Efficient energy transfer in *in₂se₃ – mos₂* van der waals heterostructures, *ACS Omega* 3 (2018) 11930–11936.
- ²⁴ A. M. v. d. Z. S. M. Nahid, S. Nam, epolarization field-induced photovoltaic effect in graphene/ $\alpha - \text{in}_2\text{se}_3$ /graphene heterostructures, *ACS Nano* 18 (2024) 14198–14206.
- ²⁵ T. Q. X. Chen, K. Xu, *et al.*, Bulk photovoltaic effect in a two-dimensional ferroelectric semiconductor $\alpha - \text{in}_2\text{se}_3$, *Nanoscale* 17 (2025) 5005–5011.
- ²⁶ J. X. A. Y. Lu, H. Zhu, *et al.*, Janus monolayers of transition metal dichalcogenides, *Nature Nanotech* 12 (2017) 744–749.
- ²⁷ A. E.-R. Z. Gan, I. Paradisanos, *et al.*, Chemical vapor deposition of high-optical-quality large-area monolayer janus transition metal dichalcogenides, *Adv. Mater.* 34 (2022) 2205226.
- ²⁸ N. S.-S. L. H. Z. P. Su, H. Ye, Second harmonic generation in janus transition metal chalcogenide oxide monolayers: A first-principles investigation, *Nanomaterials* 13 (2023) 2150.
- ²⁹ L. Q. Y. Hou, F. Xue, *et al.*, Multifunctional two-dimensional van der waals janus magnet cr-based dichalcogenide halides, *npj Comput Mater* 8 (2022) 120.
- ³⁰ Y. A. C. Li, Two-dimensional ferromagnetic semiconductors of rare-earth janus 2h-gdibr monolayers with large valley polarization, *Nanoscale* 15 (2023) 8304–8312.
- ³¹ Y. Z. P. Wang, H. Liu, *et al.*, Two-dimensional *in₂x₂x'* (x and x' = s, se, and te) monolayers with an intrinsic electric field for high-performance hotocatalytic and piezoelectric applications, *ACS Applied Materials & Interfaces* 13 (2021) 34178–34187.
- ³² J. H. G. Kresse, Ab initio molecular dynamics for liquid metals, *Phys. Rev. B* 47 (1993) 558–561.
- ³³ M. E. J. P. Perdew, K. Burke, Generalized gradient approximation made simple, *Phys. Rev. Lett.* 77 (1996) 3865–3868.
- ³⁴ M. E. J. Heyd, G. E. Scuseria, Hybrid functionals based on a screened coulomb potential, *The Journal of Chemical Physics* 118 (2003) 8207–8215.
- ³⁵ D. J. G. Kresse, From ultrasoft pseudopotentials to the projector augmented-wave method, *Phys. Rev. B* 59 (1999) 1758–1775.
- ³⁶ J. W. J. Taylor, H. Guo, Ab initio modeling of quantum transport properties of molecular electronic devices, *Phys. Rev. B* 63 (2001) 245407.
- ³⁷ B. L. D. Waldron, P. Haney, *et al.*, Nonlinear spin current and magnetoresistance of molecular tunnel junctions, *Phys. Rev. Lett.* 96 (2006) 166804.
- ³⁸ Y. J. P. P. Y. Ma, A. Kuc, *et al.*, Two-dimensional haecelite nbs(2) : A diamagnetic high-mobility semiconductor with nb(4+) ions., *Angew Chem Int Ed Engl.* 56 (2017) 10214–10218.
- ³⁹ H. Y. J. Z. Y. X. J. Chen, H. Sun, Ferroelectric in₂se₃-modulated polymorph recognition in tetralayer graphene,

- ⁴⁰ Journal of Applied Physics 137 (2025) 124301.
- ⁴⁰ Y. F. M. X. R. D. L. Ma, L. Yang, *et al.*, Observation of room-temperature out-of-plane switchable electric polarization in supported 3r-mos₂ monolayers, SmartMat 4 (2023) e1161.
- ⁴¹ H. T. O. B. C. da Silva, O. D. D. Couto, *et al.*, Optical absorption exhibits pseudo-direct band gap of wurtzite gallium phosphide, Scientific Reports 10 (2020) 7904.
- ⁴² J. L. J. Liu, W. Zhou, *et al.*, Photoinduced charge-carrier generation in epitaxial mof thin films: High efficiency as a result of an indirect electronic band gap?, Angewandte Chemie International Edition 54 (2015) 7441–7445.
- ⁴³ D.-X. Y. M.-R. L. J. Yang, Z. Sun, High-throughput screening of stable sulfide semiconductors for solar cell conversion†electronic supplementary information (esi) available, Materials Advances 5 (2024) 3904–3914.
- ⁴⁴ W. S. J. Bardeen, Deformation potentials and mobilities in non-polar crystals, Phys. Rev. 80 (1950) 72–80.
- ⁴⁵ H. Y. Q. Wang, Y. Liang, *et al.*, Universal co-existence of photovoltaics and ferroelectricity from a two-dimensional 3r bilayer bx (x = p, as, sb), J. Mater. Chem. C 10 (2022) 1048–1061.
- ⁴⁶ J. C. L. Zhang, K. Gong, *et al.*, Generation and transport of valley-polarized current in transition-metal dichalcogenides, Phys. Rev. B 90 (2014) 195428.
- ⁴⁷ Y. Z. L. L.-H. G. Y. Xie, L. Zhang, Photogalvanic effect in monolayer black phosphorus, Nanotechnology 26 (2015) 455202.
- ⁴⁸ L. E. Henrickson, Nonequilibrium photocurrent modeling in resonant tunneling photodetectors, J. Appl. Phys. 91 (2002) 6273–6281.
- ⁴⁹ N. J. R. B. Jacobs-Gedrim, M. Shanmugam, *et al.*, Extraordinary photoresponse in two-dimensional *in₂se₃* nanosheets, ACS Nano 8 (2014) 514–521.
- ⁵⁰ Z. T. Y. Wang, Z. Zhouxiaosong, *et al.*, Sliding ferroelectricity induced ultrafast switchable photovoltaic response in inse layers, Advanced Materials 36 (2021) 2410696.
- ⁵¹ W. L. T. Tong, Y. Gan, *et al.*, Boosting the sensitivity of wse2 phototransistor via janus interfaces with 2d perovskite and ferroelectric layers, ACS Nano 17 (2023) 530–538.